Self-Assembly of Twisted Monolayer Cholesteric Films via Surface Tension Local Anisotropy

Michel Mitov, Cécilia Boyon, Vanessa Soldan

Accepted version published in: *ACS Applied Nano Materials*, 5, 10560–10571 (2022)

Self-Assembly of Twisted Monolayer Cholesteric Films via Surface Tension Local Anisotropy: Implications for Multicolor Optical Tags

Michel Mitov*, Cécilia Boyon, and Vanessa Soldan†

Centre d'Elaboration de Matériaux et d'Etudes Structurales, CEMES, CNRS,

29 rue Jeanne-Marvig

F-31055 Toulouse cedex 2, France.

*Corresponding author: mitov@cemes.fr

†Centre de Biologie Intégrative, CBI, Microscopie Electronique Intégrative, METi, CNRS,

University of Toulouse

118 route de Narbonne

F-31062 Toulouse cedex, France.

Accepted version published in: *ACS Applied Nano Materials*, 5, 10560–10571 (2022)

ABSTRACT: Colorful, cholesteric patterns are ubiquitous in the bodies of insects and fishes. Bioinspired materials may be employed in smart coatings for optical communication, signaling, and camouflage. However, due to the fundamental challenges associated with such application, the development of adaptive monolayers with continuous, hierarchical nanoscale and micrometer-scale structures, as found in nature, and design simplicity has not been fully explored. We show that controlling the local anisotropy of surface tension during the self-assembly of a twisted cholesteric oligomer can lead to the appearance of distinct coexisting colors in monolayer films. The reflection wavelength, which is proportional to the helical pitch, is tuned by forming transparent, surface-active films on the free side of a cholesteric film with a pitch gradient. Reflective colors are related to the internal nanoscale structure, as demonstrated by transmission electron microscopy. Open and self-sustaining bicolor tags are created. The surface design of these films allows the manipulation of their bulk chiral self-organization on a variety of substrates. Smart, reflective multicolor tags, including self-guiding systems for autonomous vehicles, functional facades, camouflage skins for robots, and anti-counterfeiting labels, are the intended application.

KEYWORDS: self-assembly, patterning, photonics, structural color, optical tags.

https://pubs.acs.org/doi/10.1021/acsanm.2c01901

Article history:

Received: May 02, 2022.

Accepted: July 25, 2022.

Published: August 02, 2022.

1. INTRODUCTION

1.1. Patterned armor in nature. Animals control the shape, size, color and reflectivity of their bodies[1-5]. Iridescent patterns may be encountered in the armor of many insects[6-9] (Figure 1a) and fishes[10-13] (Figure 1b) with a twisted, cholesteric liquid crystal (CLC) organization of chitin or collagen (Figure 1c). Their cuticles or scales include patterns such as stripes, spots, pixels and many other shapes. The proposed functions of these patterns include communication with congeners or predators, camouflage, thermal regulation, and other functions[14]. The present work takes its inspiration from nature to find experimental means to produce patterns in iridescent monolayer films that self-organize as a consequence of the generation of periodic and differential surface tension.

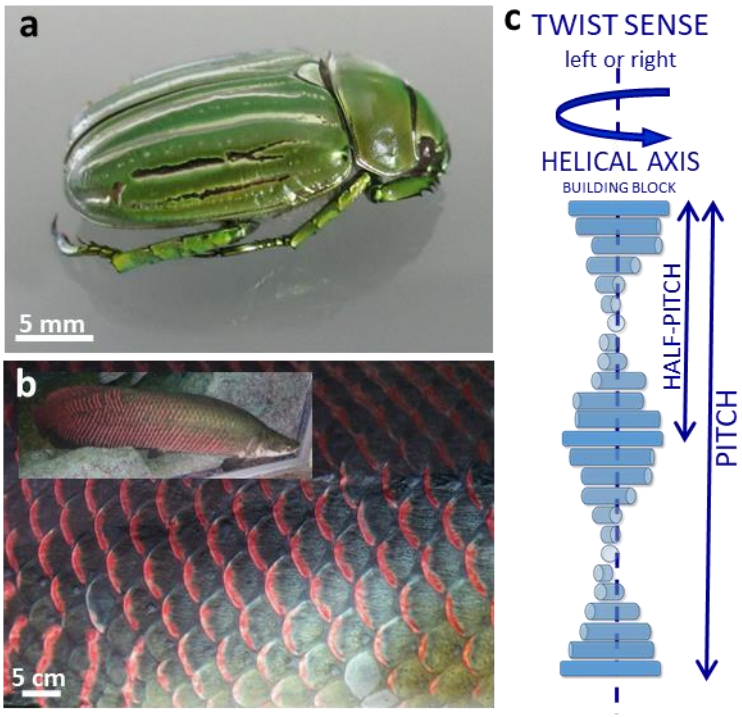

Figure 1. Cholesteric patterned armors in nature. (a) Green-and-silver striped cuticle of the scarab beetle *Chrysina gloriosa* (image by M. Mitov). (b) Red-and-dark patterns in the scales of the dermal armor of the fish *Arapaima gigas* (from 2.0 to 4.5 m long) found in the Amazon Basin. (image by Pelican, CC BY-SA 2.0. An estimate of the scale bar has been added by the authors.

Inset: image by E. Bjørtvedt, CC BY-SA 3.0). (c) Cholesteric structure schematized on the nanoscale of a single pitch. The elementary cylindrical building block represents a single molecule of a low-molecular-weight thermotropic liquid crystal, either a bundle of parallel sclerotized chitin-protein fibrils for insects or a bundle of parallel mineralized collagen-hydroxyapatite fibrils for fishes.

1.2. Main physical properties of cholesteric liquid crystals. In the CLC phase, the director of the elementary, anisotropic constituents (often a rod-like molecule in thermotropic CLCs) precesses orthogonally and continuously in a single direction, producing a self-organized helical structure[15,16]. One full rotation of the director describes the helical pitch (Figure 1c). The CLC structure repeats periodically over a distance equal to the half-pitch because of the inversion symmetry of the director. The CLC phase is also referred to as the chiral nematic LC phase; in the (achiral) nematic phase, molecules have no positional order but, on average, maintain long-range directional order with their long axes parallel. The CLC structure is ubiquitous in *in vivo* and *in vitro* biological matter[14] due to the organization of DNA and chromatin, chitin, collagen or cellulose. The helical structure of the CLC phase may exhibit a Bragg band, provided that the wavelength of the incident light matches the helical periodicity. A band gap arises from interference effects as light propagates through the CLC. At normal incidence, the mean reflection wavelength λ_0 is related to the helical pitch p by Bragg's law, $\lambda_0 = np$, where n is the average refractive index of the medium ($n=(n_{||}+n_{\perp})/2$, and $n_{||}$ and $n_{\perp}$ refer to the parallel and perpendicular components of the refractive index relative to the local director, respectively). The bandwidth of the reflection band $\Delta\lambda$ is proportional to p and the birefringence Δn: $\Delta\lambda = \Delta n\, p$, where $\Delta n = n_{||} - n_{\perp}$. Linearly polarized light that is incident parallel to the helix axis can be considered two circularly polarized waves with opposite handedness. Reflection of light in the Bragg band occurs in the circularly polarized mode matching the rotational sense of the helix. For the other circularly polarized mode with opposite handedness, light is transmitted. This second rule is associated with

selectivity in polarization: the sense of circular polarization corresponds to the screw sense of the helix, which means that a CLC structure reflects at most 50% of ambient unpolarized light in the Bragg band.

1.3. State of the art in cholesteric patterning. Challenging applications of multicolored, cholesteric monolayers with patterns visible at the human scale and versatile properties depending on their internal nanoscale structure are pending. Innovative perspectives to address the demands of society have been highlighted in recent reviews[17-21] and are related to optical signaling in functional facades, smart optical coatings to guide infrastructure for autonomous vehicles and on the body of these vehicles, or camouflage skins for robots and anticounterfeiting labels. Photoalignment by focusing a laser beam produced an 8-mm diameter green spot in red surroundings in a CLC film doped with an azo dye[22]. By stacking CLC layers with different pitches[23,24] and applying an external electric field[25], a laser beam[26] or light-driven molecular switches[27,28] can reveal colored patterns. Main-chain CLC elastomers were specifically synthesized to create a stretchable monodomain membrane and exploit its large Poisson effect in a localized, pixelated configuration by taking advantage of their mechanochromic response[29]; the pixelated structural coloration platform consisted of a base with air channels, a supporting layer, and the membrane, which is pneumatically actuated at a given pressure. Most studies have used CLC spheres embedded in an isotropic matrix in which composites are produced by microfluidics[30-32], emulsification[33,34], photopolymerization-induced phase separation in a polymer-dispersed LC (PDLC) material[28] or dispersion of CLC droplets in a PVA solution and water evaporation to change their shape[35]. Pattern formation was enabled with a magnetic field-assisted assembly of microshell arrays[30], a photomask[27,28,33], 3D printing[35], pressure[28], brush-painting and pressure[34], filling in a pixelated, polymer mold[29,32] or polymerized CLC shells manually organized in the resin binder[31].

1.4. Scientific motivation of the research. Here, we report a fundamental advancement about the impact of the surface tension anisotropy on the structural pitch, as revealed by the peculiar geometry of a cholesteric polymer subjected to a time-driven pitch gradient.

The impact of surface anchoring on the structure of CLCs is well known[36]. The behavior of CLCs in thin cells with hybrid anchoring, where one substrate promotes planar orientation while the opposite substrate imposes homeotropic (perpendicular) anchoring, has been described[37]: modulation of the structure and related patterns is caused by energetic competition between the substrates and the bulk parameters. Surface alignment can control the structural color at oblique incidence: when the alignment is changed from planar to homeotropic, the wavelength is blueshifted[38-40]. However, the role of the anisotropy of the surface tension on the nanoscale pitch, especially when it is graded from the top of the slab to the bottom, and on the related reflection color is unknown. This advancement is possible because of the experimental framework of the chosen system: (i) Two individual cholesteric layers with distinct pitch ranges are put in contact, and anisotropic diffusion occurs in the direction strictly perpendicular to the films' surfaces, which is driven with time at fixed temperature. (ii) The bottom surface is a glass substrate leading to a monotonic planar orientation everywhere. (iii) The nature of the top surface is different: spaced stripes of polymer are disposed on the open surface and induce a planar orientation, whereas the film is in contact with air in between stripes, which induces a homeotropic orientation. The coexistence, at the top surface, of air and the polymer causes a difference in the surface tension γ from the top ($\gamma_{AIR\text{-}LC}$ between air and LC) to the bottom ($\gamma_{PVA\text{-}LC}$ between PVA and LC). γ becomes anisotropic from a site that remains open to the air to a site covered with PVA. This set of geometric features of the experimental cell offers the unique opportunity to generate distinct, coexisting colors in monolayer films with a single chemical composition, arising from different effective pitches in the transverse direction of the bulky film.

In addition to this conceptual advancement, and in contrast to the previously mentioned state of the art, we investigate the physical conditions needed for the formation of polymerized monolayer samples with versatile patterns of millimeter-scale features controlled by the nanoscale structure while retaining reasonable pattern duplication fidelity for smaller patterns. This is achieved via a one-stage technique based on the controlled, local adjustment of film surface tension; by tuning the annealing time of the system only to obtain different reflection wavelengths; without the requirement for the introduction of foreign molecules or particles into the chiral material or the application of an external field; and without the employment of photomasks or specialized equipment for pattern development or the shaping of single-layer films. We provide laboratory, proof-of-concept prototypes. Macroscopic views of different multicolor striped films are accompanied by light transmission and reflection measurements and an investigation of their internal structure and cross-sections at the nanoscale using transmission electron microscopy (TEM).

2. EXPERIMENTAL MATERIALS AND METHODS

2.1. Materials. LC photocrosslinkable side-chain oligomers with a siloxane backbone were obtained from Wacker-Chemie GmbH, Munich, Germany. The photoinitiator Irgacure® 907 was purchased from Ciba Specialty Chemicals Inc. The thermal polymerization inhibitor BHT was purchased from Sigma–Aldrich (W218405). Kapton sheets for spacers were provided by Micel.

2.2. Treatment of glass plates. A polyvinyl alcohol (PVA) solution layer was used as a promoter of planar alignment of the molecules in the IR film and as a sacrificial layer to obtain free-standing films after the sample was placed in water. PVA powder (P8136, Sigma–Aldrich) was dissolved at 8 wt. % in distilled water. The resulting aqueous solution was stirred and deposited on plates using a spin coater (Ossila Ltd.). A single sequence of spin-coating consisted of the deposition of 0.20 ml of solution during a program consisting of three sequences with the

following spin rates and durations: 5000 rpm@20 s, 4000 rpm@40 s, and 3000 rpm@60 s. This operation was repeated twice. The thickness of the dried film was approximately 2 μm. Finally, the film was rubbed three times with a rayon cloth (YA-20R, Yoshikawa Chemical Company, Ltd.).

2.3. Preparation of individual films. Two distinct green-reflecting and IR-reflecting CLC samples were prepared at 110°C. The green film was a blend composed of 60 wt. % blue-reflecting compound (SB) and 40 wt. % red-reflecting compound (SR). The IR film was a blend made with 15 wt. % SR and 85 wt. % nematic CL (NLC). The SB compound contains 65 wt. % oligomer **a** (Figure 2), 8 wt. % monomer **c** and 27 wt. % monomer **d**. The SR compound contains 79 wt. % oligomer **a** and 21 wt. % monomer **c**. The SN compound contains 70 wt. % oligomer **b** and 30 wt. % monomer **c**. Changing the respective pitches (reflection colors) of the individual films is similar to changing the operating range for the reflection of light by the final material (extreme values of the Bragg band, location and width of the spectral band)[41]. This parameter indicates the versatility in the design procedure demonstrated here in the case of green and IR films. Monomers **c** and **d** were added by the supplier to the oligomers to reduce their viscosity. For the CLCs, 1.0 wt. % photoinitiator **e** and 2.0 wt. % thermal inhibitor **f** were added. A 50±1-μm-thick open film of green CLC was coated with a razor blade on a 150-μm-thick untreated glass plate at 110°C. A 21±1-μm open film of IR CLC was coated with a razor blade on a 1-mm-thick PVA-treated glass plate at 110°C. The thickness of the green film was almost two and a half times the thickness of the IR film to promote the occurrence of the Bragg band in the visible spectrum. We observed that the reflectance of the large-pitch cholesteric film increased when a layer of rubbed PVA was coated on the supporting substrate. Both films were promptly removed from the heating stage after formation. After they returned to room temperature (RT, ~22°C), they were stored at low temperature in a refrigerator.

2.4. Preparation of bilayer cells. A set of individual green and IR films was removed from the refrigerator. Particular care was taken to prevent the formation of water droplets on their free surface; i.e., compressed air was blown on their surfaces until they returned to RT. The free surfaces of the individual films were put into contact at RT by exerting a slight pressure on the upper glass plate. Interdiffusion between both films, before crosslinking, must occur in a direction perpendicular to the film surface[41]. Gravity facilitates this process since the bilayer is positioned horizontally on a heating stage. If diffusion occurs in an oblique direction, a chemical gradient occurs in the plane of the film and may create a 2D heterogeneous color inside a stripe. The smoothness of the free surfaces of the individual films must be scratch-free. To remove one plate and obtain open films of the bilayer formed while preventing the formation of scratches on the surface of the film, the bilayer with the upper plate was kept at a low temperature in a refrigerator. The plate was quickly removed from the green film with compressed air while the cell was still frozen. The smoothness of the free surface of the film after the operation was evaluated by optical microscopy. Each bilayer was then kept at RT for 10 min before transmission characterization. Due to this delay, the orientation of the CLC at the open surface of the bilayer, close to the air, changed slightly (the air induced a tilt of the director relative to its surroundings; the importance of the texture change is time-dependent[38]). As a consequence, a typical shift of the Bragg band occurred in the visible spectrum from 500 to 550 nm with respect to the individual green layer.

2.5. Formation of PVA stripes on the free surface of bilayers. Using a syringe, a drop of the PVA solution (8 wt. %) was deposited on the glass substrate supporting the bilayer film. The PVA stripe was shaped by gently moving the drop with compressed air. The width of the stripe depended on the size of the droplet. We selected this manual process leading to stripes of different shapes and widths between them to mimic the irregular stripes in the cuticle of *C. gloriosa* (Figure 1a) and to simplify the design procedure. A regular printing of the polymer and according to pre-established patterns could be obtained by printing, use of a mask during a spin-coating step of

the polymer solute or conventional lithography methods. This procedure is not the innovative part of the concept. R&D activities are beyond the scope of this fundamental study. After drying at RT for 45 min, annealing at 60°C (for 15 min or 4 h) and polymerization at 60°C for 10 min, the thickness of the PVA stripe was measured with a digital micrometer to be approximately 3 μm.

2.6. Polymerization conditions. Before polymerization, the striped material with parts in contact with air was covered by spin-coating (one run) with a 10-μm-thick layer of PVA solution (20 wt. % in water) and dried for a few seconds at RT. The purpose of this last stage was to allow polymerization and crosslinking with UV light without inhibition by oxygen. The films were placed at 60°C on a heated stage and irradiated with UV light for 10 min with a maximum intensity of 1 mW/cm^2 at 365 nm. The individual IR film (inset in Figure 4d) was irradiated at 60°C for 10 min.

2. 7. Inclusion of synthetic samples for ultramicrotomy. To obtain free-standing films ready for embedding in a piece of resin, each sample was placed in a vial of distilled water for 1 day. Due to the presence of a water-soluble PVA layer, the films detached as a block from the plates while maintaining clear-cut surfaces, as verified by TEM transverse views. A small piece of material was embedded in EMbed–812 resin (Electron Microscopy Sciences), which was then cured at 62°C for 2 days.

2.8. Preparation of samples for TEM by ultramicrotomy. A diamond knife at ambient temperature was used to cut 150-nm-thick ultrathin slices with a Leica UCT ultramicrotome. The material was cut perpendicular to the film surface (cross-sections). Slices were placed on single-slot Formvar-coated copper grids (GS2x1-C3, Gilder Grids Ltd.).

2.9. TEM conditions. A Jeol JEM–1400 microscope operating at 80 kV equipped with a Gatan Orius SC1000B CCD camera was used.

2.10. Periodicity profiles obtained from TEM images. Quantitative image analysis was performed with DigitalMicrograph software from Gatan. The intensities of the gray levels on a

given surface of the images (typical surface = 18 μm^2) were analyzed using the Profile option. The distance between two consecutive positive or negative peaks corresponded to the distance between two successive stripes of the same contrast in the fingerprint texture. Positive (negative) peaks correspond to bright (dark) stripes because the transmitted light is higher (lower) in bright dark) stripes. Peaks corresponding to intensity changes related to noisy peaks for which the measurement was questionable were excluded from the analysis (this explains why experimental points are sometimes lacking in Figure 5c and Figure 7c).

2.11. Optical micrographs. Textures were photographed with an Olympus BX51 stereomicroscope equipped with an Olympus DP73 digital camera. A 50x objective with a numerical aperture (NA) of 0.50 was used.

2.12. Optical measurements. The spectra were collected at RT and normal incidence with unpolarized incident light. A halogen source HL-2000 from Mikropack GmbH emitting from 360 nm to 1700 nm and an HR2000CG-UV–NIR spectrophotometer from Ocean Optics were used for the transmittance spectra. A Cary 5000 UV–Vis-NIR spectrometer from Varian was used for transmittance spectra, including part of the IR spectrum. The reflectance spectra were collected by placing the sample on the stage of an XploRA confocal microscope from Horiba coupled to an Olympus BX51 microscope. A 50x objective with a numerical aperture (NA) of 0.50 was used. Baselines were recorded with air (a mirror) in the beam path for transmittance (reflectance) measurements.

3. RESULTS

3.1. LC mixtures. We used photopolymerizable and crosslinkable LC oligomers with a siloxane backbone (Figure 2a and b)[42].

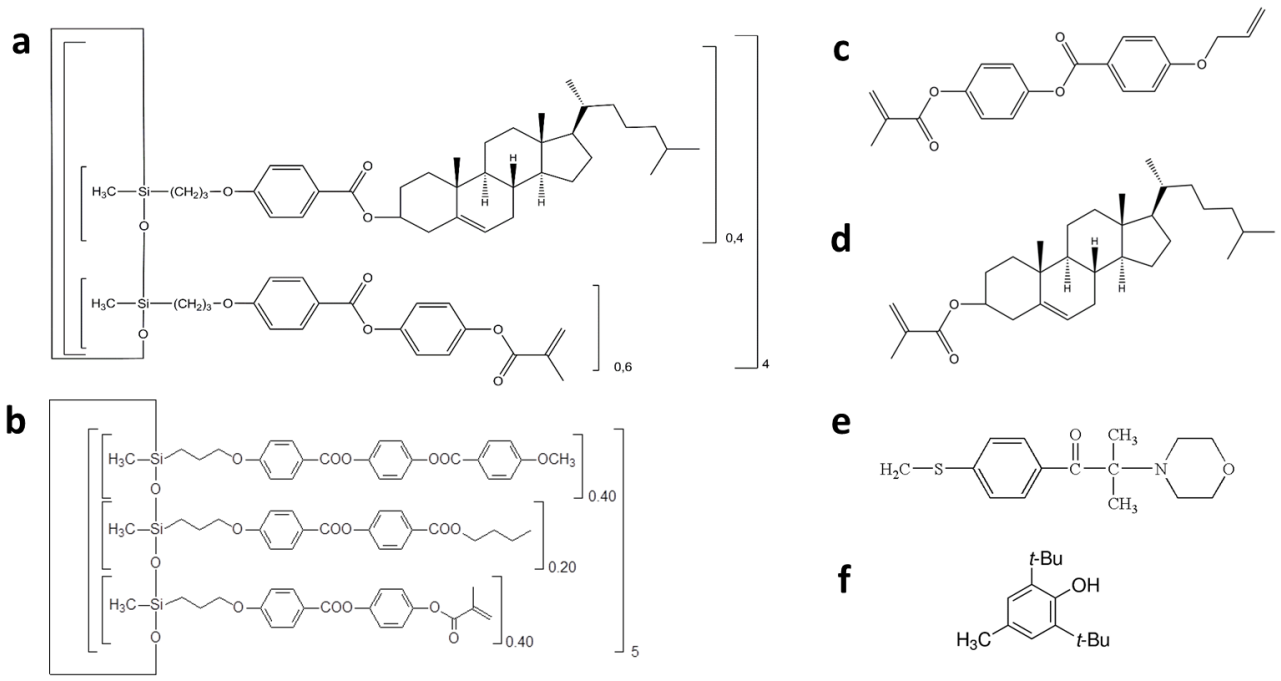

Figure 2. Structures of chemicals. Photopolymerizable and crosslinkable (a) cholesteric and (b) nematic LC siloxane-based oligomers. (c) and (d) Functional monomers. (e) Photoinitiator. (f) Thermal inhibitor.

Two types of side chains were attached via aliphatic spacers to a cyclic siloxane ring: an achiral mesogen and a chiral cholesterol-bearing mesogen (Figure 2a) or only achiral mesogens (Figure 2b). The oligomers exhibited low viscosities as a result of the low degree of polymerization. When formed as a thin film with a planar texture (the helical axis was perpendicular to the film surface), the reflected color of the cholesteric oligomer ranged from blue to red in relation to the molar percentage of chiral mesogens in the molecule and the ring size. The helical structure was left-handed. The glassy transition temperature was approximately 0°C. Polymerizable oligomers do not require a higher glass transition temperature like vitrifying oligomers (40–55°C), but the orientation of the mesogenic side chains requires a low bulk viscosity for processing to facilitate their spreading on a plate to form thin films[42]. The clearing temperature was 140°C. The

experimental cell included two CLC layers separately reflecting green and IR light (Experimental Materials and Methods).

3.2. Experimental cell. The anatomy of the cells is shown in Figure 3a. The free sides of two layers of green and IR CLCs were opposite and parallel, and they adhered via their soft interfaces at RT. Several stripes (typically two) of a solution of polyvinyl alcohol (PVA, 8 wt. %) in water were deposited on the free surface of the bilayer on the green side (Experimental Materials and Methods). The role of the polymer stripes on the top of the open film was to induce different surface energies with regard to the surface energy of the air or glass and, thus, to create different anisotropies of the surface energy from the polymer to the glass and from air to the glass. The bilayers with soft stripes were kept at RT for 45 min to allow the complete evaporation of water before continuing to process the bilayers. Each bilayer was then annealed on the heating stage at 60°C for either a *short* time of 15 min or a *long* time of 4 h, revealing the coexistence of two different colors in a single layer.

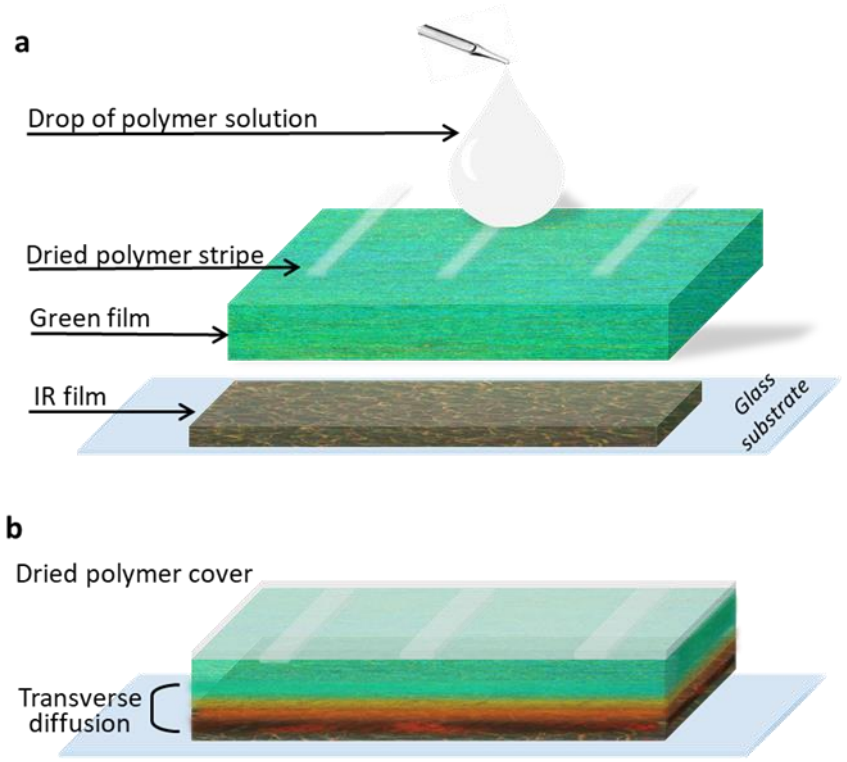

Figure 3. Anatomy of the experimental cell. (a) Stripes of polymer solution formed on the free surface of the bilayer film (green side) and dried at RT. A drop of polymer solution ready to be spin-coated is represented after transverse diffusion between the films and before UV-induced polymerization and crosslinking. (b) The experimental cell in its final state: diffusion occurred at 60°C for a variable time, and then the single-layer film was covered by spin-coating with the polymer solution. After drying at RT, the free surface was protected from oxygen, which is a polymerization inhibitor. Polymerization and crosslinking finally occurred at 60°C.

Annealing has several consequences: (1) A chemical gradient is generated between the two layers in a direction perpendicular to the film surfaces, which produces a physical pitch gradient in the transverse direction. The generation of pitch-gradient cholesterics has been carefully investigated and discussed[43-46], and the modeling of the reflection wavelength with respect to the pitch in the case of a graded twist has been addressed several times[47-50]; these results are beyond the scope of this study. (2) A homeotropic orientation of molecules is induced perpendicular to the bilayer surface surrounding the green film–air interface between two consecutive polymer stripes while the planar orientation below the stripes is maintained (Supporting Information: On the polygonal texture). (3) The bilayer material is transformed into a single layer (Experimental Materials and Methods). We provide a fourth consequence, which is precisely the subject of this paper: the generation of different pitch behaviors—profile, amplitude and gradient—in planar and homeotropic stripes, which coexist in a unique layer.

Then (Figure 3b), the striped material was covered by spin-coating (one run) with a 10-μm-thick layer of PVA solution (20 wt. % in water) and maintained at RT for a few seconds (the uniformly thin and flat liquid polymer film quickly dried). The purpose of this last stage was to allow UV-induced polymerization and crosslinking to occur without oxygen inhibition (Experimental Materials and Methods). The material was finally fixed into an elastomeric layer, which could be

cut in a transverse direction into 150-nm-thick slices to allow TEM imaging of the internal structure for comparison with their optical behavior.

3.3. Optical properties of the patterned film annealed for 15 min. Images of cells with different patterns and shapes after annealing for 15 min are shown in Figure 4a-c.

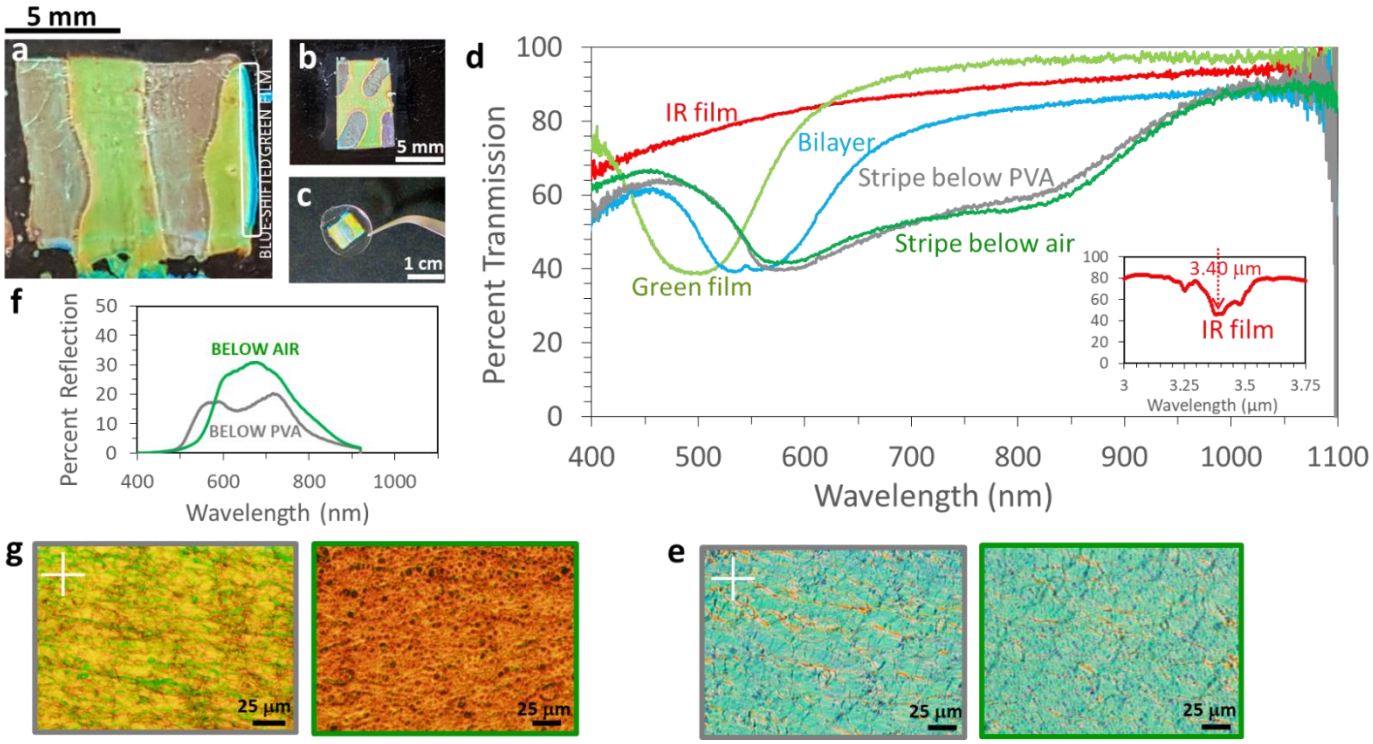

Figure 4. Patterned samples after a short annealing time (15 min): macroscopic views, optical responses and textures. (a) The free side of the film coated on a glass substrate. Black paper was placed under the cell. The right blue part of the sample corresponds to a region of the upper green film that was not in contact with the lower IR film. The color changed from green to blue as a consequence of the time-controlled tilt of the helical axis in the polygonal texture of the film in contact with air[38] (Supporting Information: On the polygonal texture). (b) Variability of the film patterning method. (c) Shaping the material as an entirely self-suspended film and then encapsulating it in a circular matrix of dried PVA solution (a clamp holds the resulting optical tag above black paper). (d) Transmission spectra of the cell shown in *a* at different stages of the design process: spectra of the green and IR individual films, the bilayer after the two films are put into contact, and the stripes below the PVA film and below the air after the final stage of polymerization.

Inset: Bragg band in the IR spectrum of the individual IR film measured after polymerization. The small peak at 3.48 μm (2873 cm^{-1}) on the right side of the reflection peak at 3.40 μm falls into the range [2850-3200 cm^{-1}] of the absorption band attributed to the C-H bond. (e) Optical textures in transmission mode of the stripes below PVA (left) and below air (right). The white cross indicates the orientation of the crossed polarizers. (f) Reflection properties: spectra of the stripes below the PVA film and below air. The wavelength scale for the representation was chosen to be the same as that used in transmission measurements. (g) Optical textures in reflection mode of the stripes below PVA (left) and below the air (right).

The surface of the cell shown in Figure 4a included two PVA-covered stripes, which appear silver (named in reference to *C. gloriosa*), and the regions between the stripes, which appear green-yellow. The pristine green layer was at the top of the bilayer, in contact with air. The pristine IR layer was coated on the substrate, which was placed on the heating stage. Figure 4b shows the variation in the design of the patterns, such as four dashed silver stripes embedded at the corners of green-yellow surroundings. If required for applications, the material could be fully detached from the supporting solid plate when covered with a water-soluble PVA layer (Experimental Materials and Methods) and included in a lump of dried PVA to become a soft tag to apply on an object (Figure 4c).

The transmission properties of the former individual layers at RT, the bilayer (after adherence of both layers) and the two kinds of stripes are shown in Figure 4d. The mean wavelength of the Bragg band of the bilayer shifted from approximately 500 nm to 550 nm compared to that of the green film (Experimental Materials and Methods). The bilayer transmission was lower than the green layer transmission because of the contribution of the optical behavior in the visible spectrum of the IR layer (attached to the green layer), which was not neutral or flat in the visible range; the bandgap of the IR film occurred at a mean transmission wavelength of 3.40 μm (inset in Figure 4d). With the exception of these two characteristics, the shapes of the Bragg bands of the green

film and bilayer were similar. Although different reflection colors could be observed by the unaided eye, the transmission bands of the stripes were similar from approximately 455 to 990 nm (when the spectrum is flat on the left and right sides of the Bragg band). Figure 4e shows the optical textures in the transmission mode of the silver (left; planar texture) and green–yellow (right; polygonal texture) stripes. In agreement with the transmission behavior, the colors were similar. In the reflection spectra shown in Figure 4f, the reflectance is displayed between 0 and 50% with regard to the polarization-selectivity rule (Introduction). The reflection of the green–yellow stripe (silver stripe) occurred at 500–900 nm (490-900 nm) when the reflectance was less than 30%. The broadened nature of the spectral bands determined from transmission and reflection was the same in both measurements. The shape of the reflection bands (flat with two bumps for the silver stripe) and the reflectance variation (reflectance two times higher than that for the green–yellow stripe) were different; these variations are discussed below in light of the volume distribution of the textural pitch from TEM images of the cross-cut material. The reflectance of the spectrum assigned to the green–yellow stripe suddenly increased from 510 to 600 nm at the maximum sensitivity of the eye to color (from 90 to 100%), which could be scaled from approximately 530 to 580 nm (Supporting Information: Reflection spectra of the silver and green stripes for an annealing time equal to 15 min versus the spectrum of human eye sensitivity). This fact, in addition to the above-reported optical behaviors, could explain why the reflection colors were perceived as different by the unaided eye, which is known to be most sensitive to green light[51]. Figure 4g shows the optical textures in the reflection mode of the silver (left; planar texture) and green–yellow (right; polygonal texture) stripes. The polygon diameter varied in the 2–7 μm range.

3.4. TEM investigation of the internal structure of the patterned film that was annealed for 15 min. TEM investigations of the polymerized film allowed us to correlate the optical

behavior of stripes to their internal twisted structure. Figures 5a and b show transverse sections of both stripes from the top to the bottom of the film.

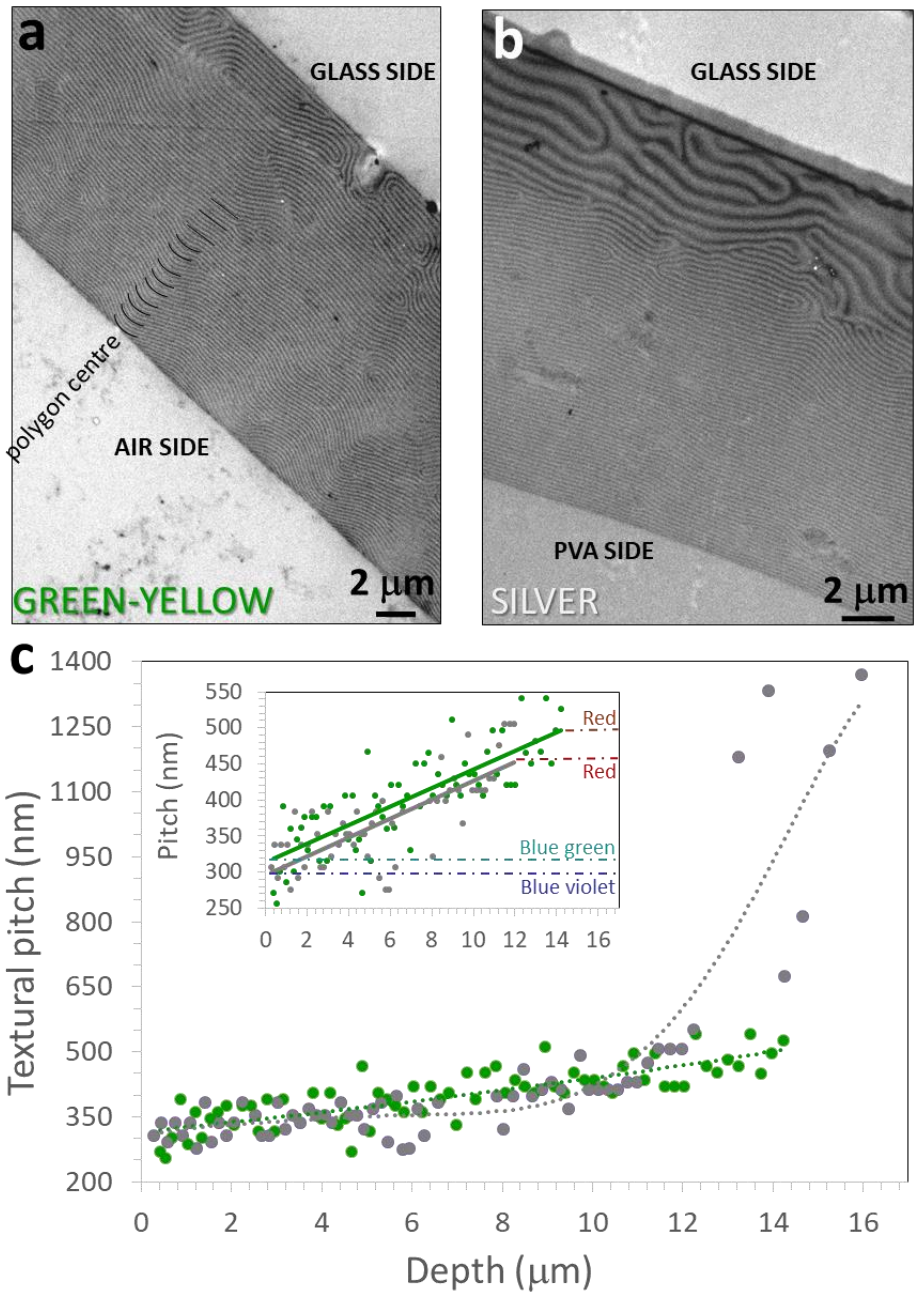

Figure 5. Structural investigation of the open sample with an annealing time of 15 min. (a) TEM transverse view of a green–yellow stripe. The perpendicular distance between two consecutive bright (or dark) lines provides an estimation of the half-pitch of the twisted structure. Arc patterns appear at the interface with air. The curvature of the arcs decreases with the depth of the cut. A few lines at different depths are partially

enhanced in black in the image. This zone corresponds to a region intercepted by the knife that is close to the center of the polygon in the plane of the film. (b) TEM transverse view of a silver stripe. The lines are parallel from the top to the bottom. (c) Textural pitch as a function of depth for both stripes. Comparison of 6th-order polynomial and linear fits. Measurements were taken at the interface with air (zero abscissa). Inset: Pitch as a function of depth when restricted to the visible spectrum. By taking 1.56 as the mean refractive index[52], the related colors are reported in the right part of the graph.

The thickness of the film was equal to 16.5±0.5 μm, as calculated from the images. TEM revealed the typical fingerprint-like texture consisting of a periodic bright-and-dark contrast[53]. This was mainly due to the mass loss during irradiation, which was selectively etched from regions in which elongated molecules were preferentially perpendicular or parallel to the imaged cut[54]. The textural pitch, the distance between two consecutive lines of the same (bright or dark) contrast, yielded an estimate of the natural half-pitch (CLC structure repeats over a distance equal to the half-pitch having head-and-tail symmetry in the local nematic director), provided that the helix could freely develop in the bulk (discussed below). An increasing pitch was visible from the top to the bottom of the two stripes. The orientation of the lines close to the air interface and the profile of the gradient differed from one stripe to the other. In Figure 5a (green–yellow stripe), the transverse view of the helical structure that corresponds to the interception of the polygonal texture is visible. Several polygonal cells were cut at different locations of their extension. The textural signature was the appearance of arced patterns close to the air interface, which became progressively straighter with the depth of the cut, up to ~8.5 μm, because the air interface (where the molecules are spontaneously perpendicular) was increasingly less influential. The evolution of the texture from the top to the bottom, from arced to straight, is shown by enhancing a set of lines in Figure 5a in black, where one polygon in the polygonal texture (Figure 4g, right) is vertical to the plane of the film. In Figure 5b (silver stripe), the lines are straight from the top to the bottom. Strikingly,

although the material exhibited the same composition below air and below PVA, the textural pitch close to the glass substrate differed from that assigned to the green–yellow stripe. When the helix was constrained (typically when the pitch was greater than the thickness on which it developed a few turns), the textural pitch deviated from the natural pitch (discussed below). Another difference is that the orientation of lines in the fingerprint-like texture close to the glass substrate fluctuated more and included more defects (disclinations). These images show that the profile diffusion between the green and IR layers differed according to whether the film was covered with a soft substrate, such as the polymer stripe.

After this qualitative description, the variation in the pitch as a function of the depth provided a quantitative description (Figure 5c). The pitch in the green–yellow stripe changed from 250 to 540 nm across the whole thickness. The lowest values of the textural pitch (up to ~300 nm) corresponded to the average of the *effective* pitch, i.e., when the helix axis was tilted, and the periodicities were lower than when the helical axis was normal to the interface. The inset in Figure 5c shows the same variation by magnifying the values corresponding to the wavelengths in the visible spectrum. The linear fit of the pitch variation in the green–yellow stripe was slightly but systematically greater than the variation in the silver stripe. By taking an estimate of n=1.56 for the mean refractive index[52], the 320–500 nm range (limits of the linear fit) corresponded to a wavelength range of 499–780 nm (from blue-green to red). The textural pitch in the silver stripe changed with the overall thickness from 300 to 1370 nm. The linear fit of the pitch in the silver stripe changed from 300 to 450 nm, corresponding to a wavelength range of 468–702 nm (from blue–violet to red). In summary, the periodicity limits corresponded to similar transmission colors in the visible spectrum, and the fits between the limits were close in value and shape. The important difference was the diverging periodicity present in the silver stripe up to 1370 nm, with related wavelengths outside the visible spectrum. This divergence was sharp and occurred over a short distance of approximately 2–3 μm (from 13.2 to 15. 9 μm); it did not make a significant

contribution to the reflection in the IR spectrum. The reflectance indeed depended on the number of helix turns for a given pitch, indicating that the twist needs to develop within a minimal film thickness to enable the appearance of a Bragg peak that is detectable under standard spectrophotometry conditions[55]. In terms of the reflectance level, we also noticed from linear fits of pitches in the visible spectrum that the fit for the silver stripe was interrupted at a depth of 12 μm, approximately 2 μm before the end of the fit for the green stripe. This could explain why the reflectance level of the silver stripe was below that of the green stripe (~10%): the *silver helix* needed to increase in thickness to develop with a level of reflectance comparable to that of the *green–yellow helix*.

3.5. Optical properties of the patterned film annealed for 4 h. Figure 6a shows an image of the patterned material as a self-sustaining film disposed on a black substrate when the annealing time was 4 h. By using only longer annealing times, the impact on the reflection colors was different. The colors were yellow–green (below dried PVA—instead of silver) and dark red (below air—instead of green–yellow). The upper part of the film was cut with a razor. In the lower part, a shift in the length of the two kinds of stripes was visible: for the yellow–green stripe, the material was bilaterally confined between two solid substrates (one soft, one hard), and its spreading appeared to be more limited than for the unilaterally confined, red stripe. On the right side, we observed that a portion of the green film was not in contact with the IR film that turned bluer for the same reason given in the case of 15 min annealing.

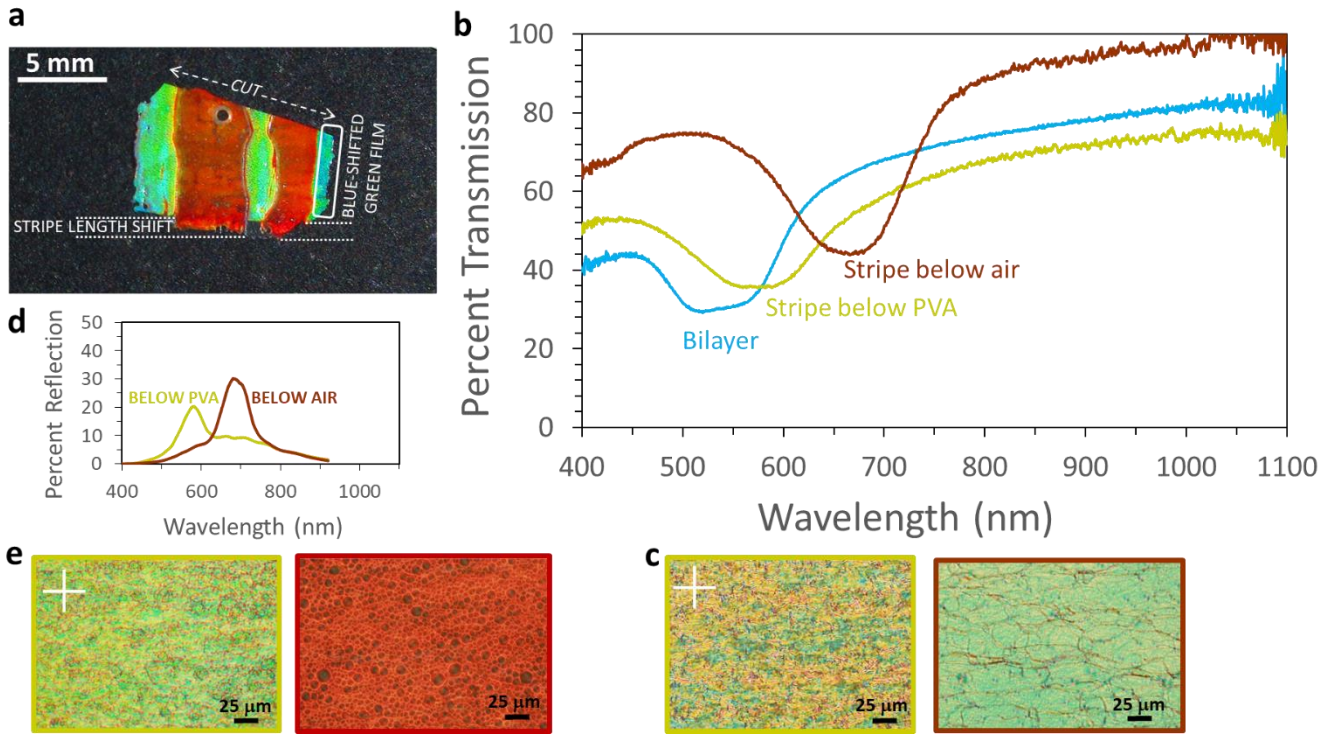

Figure 6. Patterned sample after a long annealing time (4 h): macroscopic view, optical responses and textures. (a) Striped sample as a self-sustaining film placed on black paper. The upper part of the sample was cut with a razor. The right blue part of the sample corresponds to a region of the upper green film that was not in contact with the lower IR film. Its color shifted from green to blue as a consequence of the tilt of the helical axis in the polygonal texture of the film in contact with air[38] (Supporting Information: On the polygonal texture). The lower part of the sample shows that the two reddish stripes in contact with air during annealing were longer than the two yellow–green stripes with a dried PVA layer above (*stripe length shift*). This observation provides experimental evidence that the presence of the upper PVA film limited the lateral spreading of the concerned regions. (b) Transmission spectra of the bilayer after the individual films were put into contact, the stripes below the PVA film and below air after the final stage of polymerization. (c) Optical textures in transmission mode of the stripes below PVA (left; related to the silver stripe when the time was 15 min) and below the air (related to the green–yellow stripe when the time was 15 min). The white cross indicates the orientation of the crossed polarizers. (d) Reflection properties: spectra of the stripes below the PVA film and below air. The wavelength scale for representation was the same as that in

transmission measurements. (e) Optical textures in reflection mode of the stripes below PVA (left) and below air.

The transmission properties of both kinds of stripes and the pristine bilayer are shown in Figure 6b. The mean Bragg wavelength of the bilayer was close to 540 nm. The mean wavelengths of the spectra became separated: 580 nm (yellow–green) for the stripe below PVA versus 670 nm (dark red) for the stripe below the air. Figure 6c shows the optical textures in the transmission mode of the yellow-green stripe (left; planar texture) and the red stripe (right; polygonal texture), which exhibited distinct transmission colors. The reflection spectra are shown in Figure 6d: the reflection of the yellow–green stripe was broad, including two levels of transmittance, from 450 to 900 nm, with a main peak at 580 nm; the red peak was centered at 690 nm. The bicolor nature of the single layer was clear. The optical textures in the reflection mode in Figure 6e were accompanied by yellow-green (left; planar texture) and red (right; polygonal texture) stripes. The polygon diameter was larger, varying in the 2–14 μm range (*vs.* the 2–7 μm range for the 15 min case). As expected[38], the lateral dimensions of the polygons increased with the annealing time.

3.6. TEM investigation of the internal structure of the patterned film that was annealed for 4 h. Figures 7a and b show transverse sections of both stripes from the top to the bottom of the film. The thickness of the material was equal to 19.0±1.0 μm, as calculated from the images.

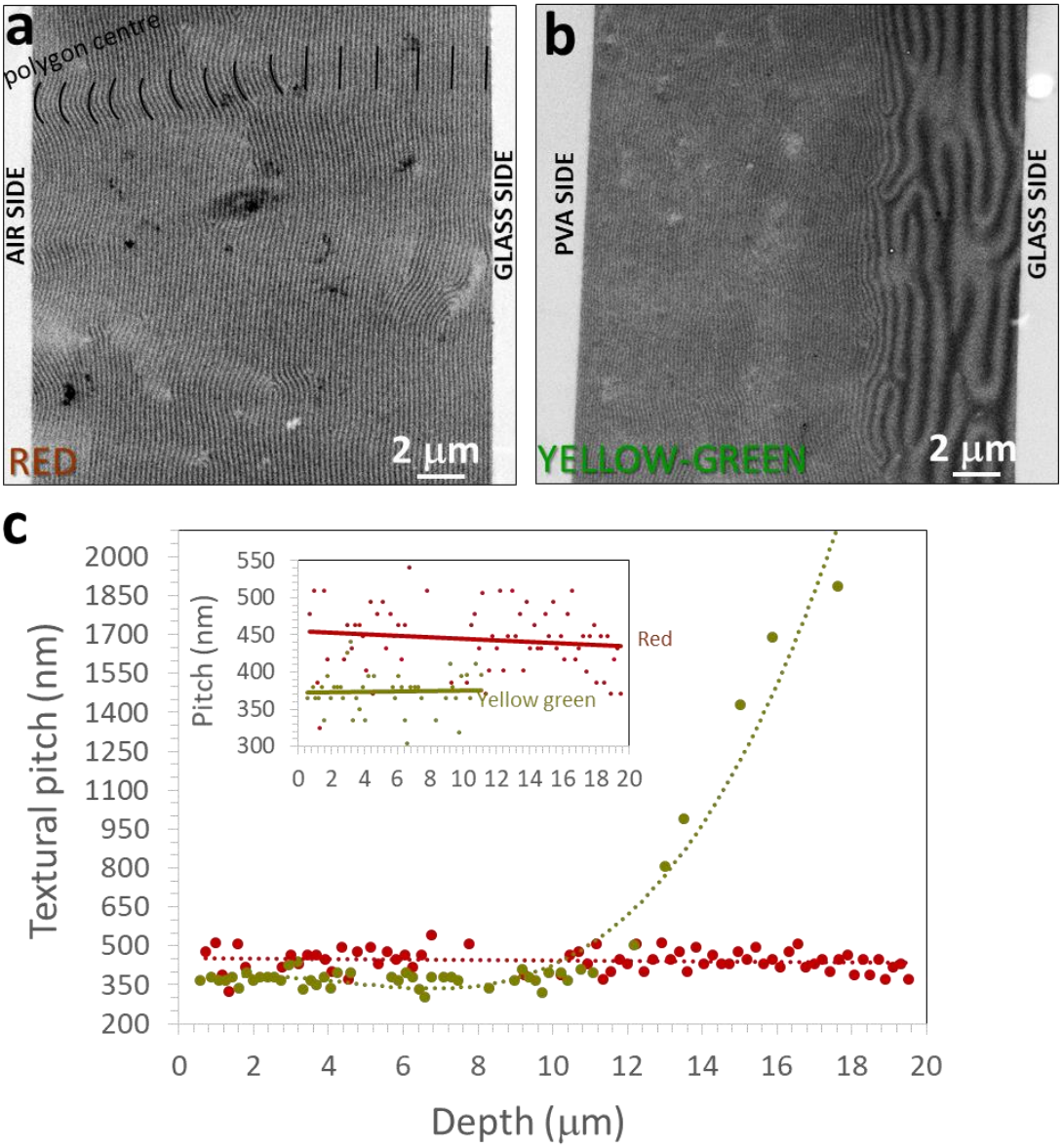

Figure 7. Structural investigation of the open sample with an annealing time of 4 h. (a) TEM transverse view of a red stripe. The distance between two consecutive bright (or dark) lines provides an estimation of the half-pitch of the CLC structure. Arc patterns were observed from the interface with air. Their curvature decreased with the depth of the cut. A few lines at different depths were partially enhanced in black. This zone corresponds to a region intercepted by the knife that is close to the polygon center in the plane of the film. (b) TEM transverse view of a yellow–green stripe. The lines are parallel from the top to the bottom. (c) Textural pitch as a function of the depth for both stripes (3rd-order polynomial and linear fits).

Measurements were taken from the interface with air (zero abscissa). Inset: Pitch variation as a function of depth if restricted to the visible spectrum. By taking 1.56 as the mean refractive index[52], the related colors are reported in the right part of the graph.

A mean pitch at 430–460 nm (inset in Figure 7c) occurred across the whole thickness of the red stripe (below air). There was an increasing textural pitch for the yellow–green stripe from 370 nm to 1890 nm (Figure 7c); the divergence began at 12 μm by sharply expanding from 6 μm out of the visible range to the end of the portion of the film, close to the glass side, where fluctuations and defects were visible in the distribution of lines intrinsic to the fingerprint-like texture (Figure 7b). In summary, the distinct elements between the two kinds of stripes are the orientation of lines close to the air interface (curved below air and straight below PVA), a larger pitch below the air in the visible range (430–460 nm) *vs.* 370 nm below PVA (inset in Figure 7c), and the graded nature of the pitch below PVA only. Regarding the different reflectance levels (Figure 6d), in this case, we also noticed from the linear fits of the pitch in the visible spectrum (inset in Figure 7c) that the fit of the yellow–green stripe was interrupted at a thickness of 10.5 μm, approximately 8 μm before the end of the fit for the red stripe. The *yellow–green helix* required a greater thickness to develop with a level of reflectance comparable to that of the *red helix*, whose quasi-constant pitch was allowed to develop at a greater thickness.

4. DISCUSSION

4.1. Differential nature of the surface tension at the origin of the patterned films. The anisotropy of the LC properties, such as viscosity, depends on the molecular alignment at interfaces[37]. As a consequence, anisotropic tensions at interfaces must also be considered. It is challenging to measure the surface tension γ of long-range partially ordered media, which are LCs, with classical techniques, such as the pendant drop method[56-58]. In addition, when considering the

problem, it cannot be assumed that the γ value of an LC in contact with aqueous PVA solution is identical to that of an interface with pure water, although the planar alignment is the same[58]. Unlike nematic structures that are invariant in three dimensions, cholesteric structures are complex, especially when it is necessary to know γ under different conditions of alignment and the difference in surface tension Δγ between confining surfaces. $\Delta\gamma = | \gamma^{UP} - \gamma^{DOWN} |$, where γ^{UP} is the surface tension between the upper substrate and the LC and γ^{DOWN} is the surface tension between the bottom substrate and the LC. The situation is more complicated when the molecular organization continuously changes with the depth in the material, as in this case where there is a time-dependent pitch gradient. The purpose of this section is to discuss the variation in Δγ below the PVA layer, which promotes monotonic molecular orientation tangential to the surfaces from the top to the bottom glass side, with regard to what happens below the air, which promotes a normal (homeotropic) orientation, to a tangential (planar) orientation at the bottom glass side.

For the confined uniformly planar stripe, we may expect the viscosity to be controlled by the presence of two solid surfaces (the PVA film and the glass plate) and the influence of the surface activity of PVA. The surface activity of PVA at interfaces is poorly understood[59]. Thus, conducting a quantitative analysis of the impact of the anisotropic surface energy on the color of the different patterns of the film is currently not feasible. Viscosity is a parameter of paramount importance to control diffusion between the pristine green and IR layers and depends on the twisted structure at the origin of the final structural color at the end of short- or long-term annealing. For the unilaterally confined open stripe (between the air and the glass substrate), we can reasonably assume that this part of the material experiences interlayer diffusion with more degrees of freedom than in the bilaterally confined stripe (between the PVA film and the glass substrate) due to the absence of an upper solid substrate; for an annealing time of 4 h, this stripe overflows from the initially delimited surface (Figure 6a). The twist difference from one kind of stripe to the other could result from a viscosity difference arising from a Δγ difference. This situation is enhanced at

longer annealing times. This means that the color difference and the nature of the colors can be tuned with the annealing time, whereas the chemical composition of the material and its single-layer nature are the same from one kind of stripe to the other. At this point, a distinction must be made between natural and textural pitches. The natural pitch is the free pitch, precisely determined in the absence of significant constraints, i.e., the layer thickness and the influence of surfaces: this means that the twist may develop without frustration due to sufficient material thickness that allows the free development of the helix. This situation can be described in terms of the confinement ratio C, which is defined as the total thickness to the natural pitch ratio d/p_0, which is much greater than one in this case. In summary[60], (i) when C is less than a critical value C_c, a dark zone appears in the fingerprint-like texture (here observed by TEM) where the molecules align perpendicular to the plates. The helices unwind, and the material has a homeotropic nematic-like structure. Typically, C_c is approximately equal to 1. (ii) For $C_c < C < C^*$, a fingerprint-like texture composed of lines separated by dark homeotropic nematic regions is observed. The helix deforms and partially unwinds. In current CLCs, C^* is approximately equal to 1.5[60]. C^* defines the value for which a pattern transition occurs, from birefringent fingers embedded in a dark background to fully connected fingers. (iii) When $C > C^*$, the fingers are in contact and completely form the periodic and continuous fingerprint-like texture: this case typically occurs from the PVA side (taken as zero along the abscissa) to approximately 10 μm (Figure 5b, Figure 7b); the textural pitch may reasonably be assimilated to the natural pitch. Above 10 μm, the textural pitch typically corresponds to the case of $1 < C < 1.5$ for this lowest part of the thickness: the helical structure is distorted, and the helix partially untwists in the regions where the fingerprint texture appears black. When two layers undergo time-dependent diffusion, the textural pitch—that is, the distance between two black (or clear) lines in the fingerprint-like textures—does not correspond to the local value of the natural pitch. Instead, it corresponds to a compromise between the tendency of the helices to freely develop and the local space controlling this development, which does not allow

full twisting. Instead of completely parallel aligned lines, the curvatures of the lines in the fingerprint texture next to the glass side convey this context. The self-organization of the CLC phase depends on the local geometry, which is controlled by the anisotropy of the surface tension $\Delta\gamma$ from the top to the bottom. The self-organization of the twisted structure giving rise to different structural colors is different in unilaterally and bilaterally confined stripes.

When the annealing time is short, Figure 5a (15 min) shows no more periodicity in the IR spectrum, but a pitch gradient exists from blue to red for both stripes, which indicates that the IR layer (p_0 = 3.40 μm) and the green layer were not fully blended. However, periodicities in the IR spectrum are present below PVA (Figure 5b). When the annealing time is long, there is no more natural pitch gradient, which is expected because the layers fully blend. A textural pitch in the IR spectrum is visible under PVA (Figure 7b).

In summary, $\Delta\gamma$ is conceptually different from one kind of stripe to the other and from one annealing time to another time in the same and unique cell. The paramount importance of its role in the coexistence of different colors in a single layer has been revealed in the case of transversally directed diffusion between layers with different pitches, which is controlled with time at fixed temperature. In that case, $\Delta\gamma$ allows the existence of a different pitch gradient (inset in Figure 5c) or no gradient (inset in Figure 7c), regardless of the presence (Figure 5b and Figure 7b) or absence (Figure 5a and Figure 7a) of periodicities in the IR spectrum, the degree of consumption of the IR layer, in the presence of a single layer material (in all cases), or the labile and stable coexistence of distinct reflection colors, which are fixed afterward by polymerization. Figure 8 shows a schematic of the situation for the two extreme annealing times, 15 min (Figure 8a) and 4 h (Figure 8b). LC phases typically show anisotropic alignment-dependent properties, so LCs are also thought to have anisotropic interfacial tensions; γ and $\Delta\gamma$ are differently labeled because the chemical compositions of the CLC close to the surfaces and equally the orientation of the twisted structure

(as revealed by fingerprint TEM textures) are expected to be different due to the time-controlled diffusion between the individual layers.

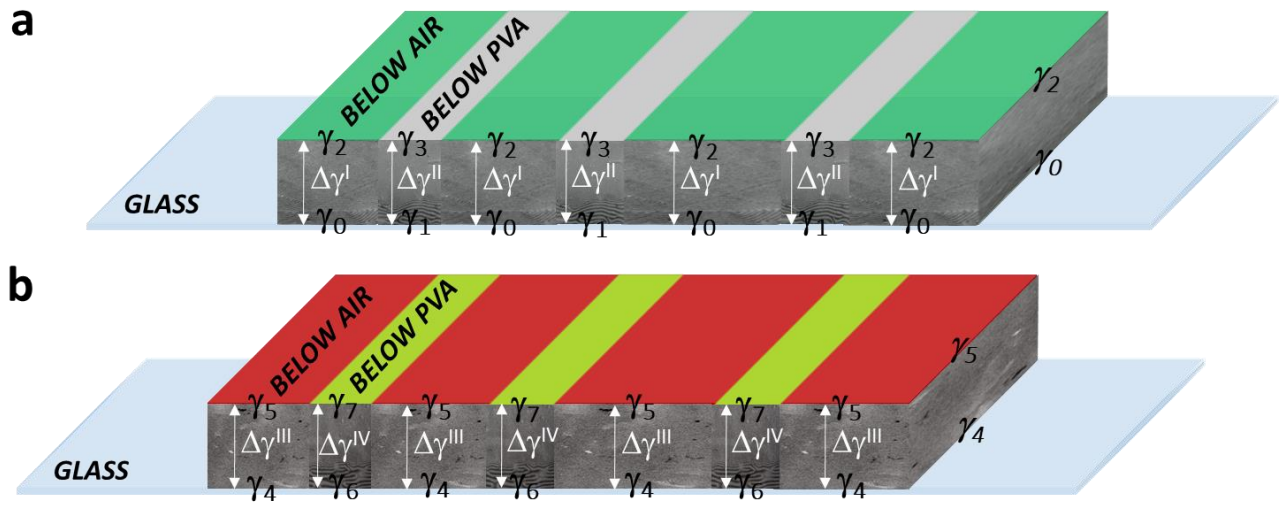

Figure 8. Schematic views of different surface tensions $\gamma_{0\ to\ 7}$ and related surface tension anisotropy $\Delta\gamma^{I\ to\ IV}$ at the origin of the patterned films. The annealing time equal is equal to (a) 15 min (green–yellow and silver colors) and (b) 4 h (red and yellow–green colors).

4.2. Practical uses and perspectives. This work provides fundamental results for bicolor films and proof-of-concept prototypes. In an R&D approach, which is beyond the objectives of the present study, it can be envisioned that polymer films with different surface activities could be used to generate more than two colors in one film. Smart, reflective multicolor tags are the intended application. Most applications of multicolor, single-layer materials with a high level of versatility and simplicity during one unique stage in their design can take advantage of patterning at the human scale. Simple solutions to modify CLC self-organization are desired when they allow the formation of films on a variety of surfaces and do not require well-defined alignment layers, the patterning of substrates, and the application of an external field or additional complex technologies.

In architecture, large multipatterned CLC coatings on infrastructure are relevant for guiding autonomous vehicles and humans to their destination. Such smart coatings could carry information that can be optically decrypted thanks to the manifold selectivity of CLCs (color, polarization, and variability with viewing angle) if they can be designed in the forms of color-changing monolayers with different shapes (planar or curved, coated on a solid or flexible substrate, self-sustainable in a transparent matrix). Only two-dimensional areas must be covered. No wiring to a physical device is required to display information by selectively reflecting defined wavelength bands and polarizations, i.e., circularly polarized light at normal incidence or elliptically polarized light at variable angles of incidence[17]. Reflective patterns might also be used on road signs for visibility, traffic warnings and advertisements[20].

Optical coatings for autonomous vehicles may support the development of self-navigating cars. If the CLC reflection is tuned to the IR range to avoid visual pollution, then an information-rich landscape may be visible only to machines designed to communicate with this part of the optical spectrum. In the field of soft robots[18,61], one of the most frequently considered polymer systems is related to camouflage skins and control systems (optical sensors and signaling) for autonomous robots.

Because of the link between the shape and the size of the polymer film and those of the developed nanoscale-controlled colored pattern, changing the surface tension of cured films via the deposition of polymer solutions through micrometer-scale masks or submicrometer size, or by lithography, could produce patterns smaller than those achieved in the present study. This may inspire applications in nanophotonics, large-angle diffraction[62] or reflection–diffusion–grating devices[63-65].

5. CONCLUSIONS

Transverse interdiffusion between two oligomer layers in the cholesteric phase and reflection of light in separate wavelength bands, namely, the green part of the visible spectrum and the IR spectrum, were monitored over time. Thin stripes of a PVA polymer film were deposited on the free surface of the bilayer system. The surface tension was changed locally from open regions to those covered by polymer films, which altered the nanoscale self-organization, as observed by TEM. Finally, the polysiloxane-based oligomeric system was solidified by UV-induced crosslinking. In the internal structure of the final monolayer, two periodicity distributions were observed in the twisted structure: with or without a gradient and with or without periodicity in the IR spectrum. Different colors coexisted in a continuously structured monolayer with a single chemical composition. The impact of the surface tension anisotropy on the bilayer geometry was revealed. Different reflection wavelengths were achieved by tuning the annealing time of the system only. In addition to the current fundamental objectives, multicolor films could be created in a unique cholesteric film utilizing distinct polymer stripes of different natures with varied surface activity via R&D methods.

ASSOCIATED CONTENT

Supporting Information

The Supporting Information (PDF) is available free of charge at:

https://pubs.acs.org/doi/10.1021/acsanm.2c01901.

- Figure S1: On the polygonal texture.
- Figure S2: Reflection spectra of the silver and green stripes for an annealing time of 15 min versus the spectrum of human eye sensitivity.
- Discussion of the comparison with glassy samples mimicking the cuticle of *C. gloriosa*.
- Supporting references.

AUTHOR INFORMATION

Corresponding Author

Michel Mitov — Centre d'Elaboration de Matériaux et d'Etudes Structurales, CEMES, CNRS, 29 rue Jeanne-Marvig, F-31055 Toulouse cedex 2, France;

orcid.org/0000-0003-1831-2152;

Email: mitov@cemes.fr

Authors

Cécilia Boyon — Centre d'Elaboration de Matériaux et d'Etudes Structurales, CEMES, CNRS, 29 rue Jeanne-Marvig, F-31055 Toulouse cedex 2, France.

Vanessa Soldan — Centre de Biologie Intégrative, CBI, Microscopie Electronique Intégrative, METi, CNRS, University of Toulouse, 118 route de Narbonne, F-31062 Toulouse cedex, France.

Author Contributions

M. M. led the conceptual development of the research, oversaw data collection, analyzed the results, organized the content of the manuscript, prepared the figures and wrote the manuscript. C. B. contributed to the development of samples, prepared samples and cells, performed optical transmission characterization, and participated in the collection of data. V. S. prepared and cut the inclusions by ultramicrotomy and conducted TEM observations. All authors approved the final version of this paper.

Notes

The authors declare no competing financial interest.

Research data are available from the corresponding author upon reasonable request.

ACKNOWLEDGMENTS

This work was financially supported by the Agence Nationale de la Recherche, France (COLEOPTIX, ANR-17-CE30-0025). M. M. thanks Dr. E. Hanelt from Wacker-Chemie GmbH (Munich, Germany) for providing oligomers. Mr. S. Moyano is acknowledged for his technical help in making reflection measurements.

REFERENCES

(1) Camazine, S., Deneubourg, J.-L., Franks, N. R., Sneyd, J., Theraulaz, G., Bonabeau, E. *Self-Organization in Biological Systems*; Princeton University Press: Princeton, 2001.

(2) Berthier, S. *Iridescences—The Physical Colors of Insects*; Springer: New York, 2007.

(3) Stevens, M., Merilaita, S. *Animal Camouflage*; Cambridge University Press: Cambridge, 2011.

(4) Luo, M., Lu, G., Yin, H., Wang, L., Atuganile, M., Dong, Z. Fish pigmentation and coloration: Molecular mechanisms and aquaculture perspectives. *Rev. Aquac.* **2021**, *13*, 2395.

(5) Stuart-Fox, D., Ospina-Rozo, L., Ng, L., Franklin, A. M. The Paradox of Iridescent Signals. *Trends Ecol. Evol.* **2021**, *36*, 187.

(6) Seago, A. E., Brady, P., Vigneron, J.-P., Schultz, T. D. Gold bugs and beyond: a review of iridescence and structural colour mechanisms in beetles (Coleoptera). *J. R. Soc. Interface* **2009**, *6*, 165.

(7) Yu, K., Fan, T., Lou, S., Zhang, D. Biomimetic optical materials: Integration of nature's design for manipulation of light. *Prog Mater Sci* **2013**, *58*, 825.

(8) Odin, G. P., McNamara, M. E., Arwin, H., Järrendahl, K. Experimental degradation of helicoidal photonic nanostructures in scarab beetles (Coleoptera: Scarabaeidae): implications for

the identification of circularly polarizing cuticle in the fossil record. *J. R. Soc. Interface* **2018**, *15*, 20180560.

(9) Lee, N., Berthelson, P. R., Nguyen, V., Garrett, M., Brinda, A. K., Moser, R. D., Horstemeyer, M. F., Rhee, H., Prabhu, R. K. Microstructure and nanomechanical properties of the exoskeleton of an ironclad beetle (Zopherus haldemani). *Bioinspir. Biomim.* **2021**, *16*, 036005.

(10) Zimmermann, E. A., Gludovatz, B., Schaible, E., Dave, N. K. N., Yang, W., Meyers, M. A., Ritchie, R. O. Mechanical adaptability of the Bouligand-type structure in natural dermal armour. *Nat. Commun.* **2013**, *4*, 2634.

(11) Yang, W., Sherman, V. R., Gludovatz, B., Mackey, M., Zimmermann, E. A., Chang, E. H., Schaible, E., Qin, Z., Buehler, M. J., Ritchie, R. O., Meyers, M. A.. Protective role of Arapaima gigas fish scales: Structure and mechanical behavior. *Acta Biomater.* **2014**, *10*, 3599.

(12) Quan, H., Yang, W., Schaible, E., Ritchie, R. O., Meyers, M. A. Novel Defense Mechanisms in the Armor of the Scales of the "Living Fossil" Coelacanth Fish. *Adv. Funct. Mater.* **2018**, *28*, 1804237.

(13) Yin, S., Yang, R., Huang, Y., Guo, W., Chen, D., Zhang, W., Ren, M., Zhou, Y., Xu, J. Toughening mechanism of coelacanth-fish-inspired double-helicoidal composites. *Compos. Sci. Technol.* **2021**, *205*, 108650.

(14) Mitov, M. Cholesteric liquid crystals in living matter. *Soft Matter* **2017**, *13*, 4176.

(15) de Gennes, P. G., Prost, J. *The Physics of Liquid Crystals*, Oxford University Press: Oxford, 1995.

(16) Collings, P. J., Goodby, J. W., *Introduction to Liquid Crystals: Chemistry and Physics*, CRC Press: Boca Raton, 2019.

(17) Schwartz, M., Lenzini, G., Geng, Y., Rønne, P. B., Ryan, P. Y. A., Lagerwall, J. P. F. Cholesteric Liquid Crystal Shells as Enabling Material for Information-Rich Design and Architecture. *Adv. Mater.* **2018**, *30*, 1707382.

(18) Wallin, T. J., Pikul, J., Shepherd, R. F. 3D printing of soft robotic systems. *Nat. Rev. Mater.* **2018**, *3*, 84.

(19) Shang, L., Zhang, W., Xu, K., Zhao, Y. Bio-inspired intelligent structural color materials. *Mater. Horiz.* **2019**, *6*, 945.

(20) Qi, Y., Zhou, C., Niu, W., Zhang, S., Wu, S., Ma, W., Tang, B. Retroreflection and Wettability Controlled Smart Indicator Based on Responsive Bilayer Photonic Crystals for Traffic Warning. *Adv. Opt. Mater.* **2020**, *8*, 2001367.

(21) Wu, P., Wang, J., Jiang, L. Bio-inspired photonic crystal patterns. *Mater. Horiz.* **2020**, *7*, 338.

(22) Lin, T. H., Huang, Y., Zhou, Y., Fuh, A. Y. G., Wu, S.-T. Photo-patterning micro-mirror devices using azo dye-doped cholesteric liquid crystals. *Opt Express* **2006**, *14*, 4479.

(23) Vicentini, F., Cho, J., Chien, L.-C. Tunable chiral materials for multicolour reflective cholesteric displays. *Liq. Cryst.* **1998**, *24*, 483.

(24) Bae, K.-S., Jang, Y.-J., Moon, Y.-K., Kang, S.-G., Cha, U., Yu, C.-J., Jang, J. E., Jung, J. E., Kim, J.-H. Multicolor Cholesteric Liquid Crystal Display in a Single-Layered Configuration using a Multi-Pitch Stabilizations. *Jpn. J. Appl. Phys.* **2010**, *49*, 084103.

(25) Hikmet, R. A. M., Polesso, R. Patterned Multicolor Switchable Cholesteric Liquid Crystal Gels. *Adv. Mater.* **2002**, *14*, 502.

(26) Saadaoui, L., Petriashvili, G., De Santo, M. P., Hamdi, R., Othman, T., Barberi, R. Electrically controllable multicolor cholesteric laser. *Opt. Express* **2015**, *23*, 22922.

(27) Wang, H., Bisoyi, H. K., Urbas, A. M., Bunning, T. J., Li, Q. Reversible Circularly Polarized Reflection in a Self-Organized Helical Superstructure Enabled by a Visible-Light-Driven Axially Chiral Molecular Switch. *J. Am. Chem. Soc.* **2019**, *141*, 8078.

(28) Cui, S., Qin, L., Liu, X., Yu, Y.. Programmable Coloration and Patterning on Reconfigurable Chiral Photonic Paper. *Adv. Opt. Mater.* **2022**, 2102108.

(29) Kim, S.-U., Lee, Y.-J., Liu, J., Kim, D. S., Wang, H., Yang, S. Broadband and pixelated camouflage in inflating chiral nematic liquid crystalline elastomers. *Nat. Mater.* **2022**, *21*, 41.

(30) Lin, Y., Yang, Y., Shan, Y., Gong, L., Chen, J., Li, S., Chen, L. Magnetic Nanoparticle-Assisted Tunable Optical Patterns from Spherical Cholesteric Liquid Crystal Bragg Reflectors. *Nanomaterials* **2017**, *7*, 376.

(31) Geng, Y., Kizhakidathazhath, R., Lagerwall, J. P. F. Encoding Hidden Information onto Surfaces Using Polymerized Cholesteric Spherical Reflectors. *Adv. Funct. Mater.* **2021**, *31*, 2100399.

(32) Qin, L., Liu, X., He, K., Yu, G., Yuan, H., Xu, M., Li, F., Yu, Y. Geminate labels programmed by two-tone microdroplets combining structural and fluorescent color. *Nat. Comm.* **2021**, 12, 699.

(33) Belmonte, A., Bus, T., Broer, D. J., Schenning, A. P. H. J. Patterned Full-Color Reflective Coatings Based on Photonic Cholesteric Liquid-Crystalline Particles. *ACS Appl. Mater. Interfaces* **2019**, *11*, 14376.

(34) Belmonte, A., Pilz da Cunha, M., Nickmans, K., Schenning, A. P. H. J. Brush-Paintable, Temperature and Light Responsive Triple Shape-Memory Photonic Coatings Based on

Micrometer-Sized Cholesteric Liquid Crystal Polymer Particles. *Adv. Opt. Mater*. **2020**, *8*, 2000054.

(35) Yang, C., Wu, B., Ruan, J., Zhao, P., Chen, L., Chen, D., Ye, F. 3D-Printed Biomimetic Systems with Synergetic Color and Shape Responses Based on Oblate Cholesteric Liquid Crystal Droplets. *Adv. Mater*. **2021**, *33*, 2006361.

(36) Dierking, I. *Textures of Liquid Crystals*, Wiley-VCH: Weinheim, 2003.

(37) Biagio, R. L., Teixeira de Souza, R., Evangelista, L. R., Zola, R. S. Role of the surface anchoring energy on the spontaneous modulated pattern formation of hybrid aligned cholesteric liquid crystals. *Mol. Cryst. Liq. Cryst.* **2017**, 657, 107.

(38) Agez, G., Bitar, R., Mitov, M. Color selectivity lent to a cholesteric liquid crystal by monitoring interface-induced deformations. *Soft Matter* **2011**, *7*, 2841.

(39) Iadlovska, O. S., Maxwell, G. R., Babakhanova, G., Mehl, G. H., Welch, C., Shiyanovskii, S. V., Lavrentovich. O. D. Tuning selective reflection of light by surface anchoring in cholesteric cells with oblique helicoidal structures. *Optics Lett.* **2018**, *43*, 1850.

(40) Lim, C., Bae, S., Jeong, S. M., Ha, N. Y. Manipulation of Structural Colors in Liquid-Crystal Helical Structures Deformed by Surface Controls. *ACS Appl. Mater. Interfaces* **2018**, *10*, 12060.

(41) Mitov, M., Binet, C., Boudet, A., Bourgerette, C. Glassy cholesteric broadband reflectors with a pitch gradient: material design, optical properties and microstructure *Mol. Cryst. Liq. Cryst*. **2001**, *358*, 209.

(42) Kreuzer, F.-H., Häberle, N., Leigeber, H., Maurer, R., Stohrer, J., Weis, J. In *Organosilicon Chem. III*; N. Auner, J. Weiss, Eds.; Wiley-VCH: Weinheim, 1997; pp. 566–586.

(43) Mitov, M. Cholesteric Liquid Crystals with a Broad Light Reflection Band. *Adv. Mater*. **2012**, *24*, 6260.

(44) Zhang, L. Y., Gao, Y. Z., Song, P., Wu, X. J., Yuan, X., He, B. F., Chen, X. W., Hu, W., Guo, R. W., Ding, H. J., Xiao, J. M., Yang, H. Research progress of cholesteric liquid crystals with broadband reflection characteristics in application of intelligent optical modulation materials. *Chin. Phys. B* **2016**, *25*, 096101.

(45) Balamurugan. R., Liu, J.-H. A review of the fabrication of photonic band gap materials based on cholesteric liquid crystals. *React. Funct. Polym*. **2016**, *105*, 9.

(46) Sun, J., Zhang, W., Wang, M., Zhang, L., Yang, H. Bandwidth Tunable Cholesteric. In: *Liquid Crystal Liquid Crystal Sensors*, A. P. H. J. Schenning, G. P. Crawford, D. J. Broer, Eds.; Taylor and Francis, 2018; pp. 1-25.

(47) Ting, C. L., Lin, T. H., Liao, C. C., Fuh, A. Y. G. Optical simulation of cholesteric liquid crystal displays using the finite-difference time-domain method. *Optics Express* **2006**, *14*, 5594.

(48) Rofouie, P., Pasini, D., Rey, A. D. Tunable nano-wrinkling of chiral surfaces: Structure and diffraction optics. *J. Chem. Phys.* **2015**, *143*, 114701.

(49) Wensink, H. H., Ferreiro-Cordova, C. Twisting with a twist: supramolecular helix fluctuations in chiral nematics. *Soft Matter* **2017**, *13*, 3885.

(50) Agez, G., Bayon, C., Mitov, M. Multiwavelength Micromirrors in the Cuticle of Scarab Beetle Chrysina gloriosa. *Acta Biomater.* **2017**, *48*, 357.

(51) Kremers, J., Baraas, R. C., Marshall, N. J., Eds, *Human Color Vision*, Springer: Switzerland, 2016.

(52) Figure 15 in Reference (42) provides the variation of refractive indexes $n_{\parallel}$ and $n_{\perp}$ before and after photocrosslinking at 70°C for the green CLC mixture as a function of temperature. We assume that the values are not significantly changed when the crosslinking occurs at 60°C (like in the present study). Measurements of both indexes after crosslinking in Figure 15 are displayed from 48°C to 100°C. The closest value to the RT (~22°C) is thus 48°C. At 48°C: $n_{\parallel}$ = 1.61 and $n_{\perp}$ = 1.51, hence a mean refractive index n = 1.56. We assume that this value is not significantly changed from the green to the IR CLC and when a gradual chemical diffusion between these compounds has occurred and is stored in a polymer film.

(53) Pierron, J., Boudet, A., Sopena, P., Mitov, M., Sixou, P. Cholesteric textures observed by transmission electron microscopy in diffraction contrast. *Liq. Cryst.* **1995**, *19*, 257.

(54) Boudet, A., Mitov, M., Bourgerette, C., Ondarçuhu, T., Coratger, R. Glassy cholesteric structure: thickness variation induced by electron radiation in transmission electron microscopy investigated by atomic force microscopy. *Ultramicroscopy* **2001**, *88*, 219.

(55) St. John, W. D., Fritz, W. J., Lu, Z. J., Yang, D.-K. Bragg reflection from cholesteric liquid-crystals. *Phys. Rev. E* **1995**, *51*, 1191.

(56) Tintaru, M., Moldovan, R., Beica, T., Frunza, S. Surface tension of some liquid crystals in the cyanobiphenyl series. *Liq. Cryst.* **2001**, *28*, 793.

(57) Kim, J.-W., Kim, H., Lee, M., Magda, J. J. Interfacial Tension of a Nematic Liquid Crystal/Water Interface with Homeotropic Surface Alignment. *Langmuir* **2004**, *20*, 8110.

(58) Honaker, L., Sharma, A., Schanen, A., Lagerwall, J. P. F. Measuring the Anisotropy in Interfacial Tension of Nematic Liquid Crystals. *Crystals* **2021**, *11*, 687.

(59) Moll, C. J., Meister, K., Kirschner, J., Bakker, H. J. Surface Structure of Solutions of Poly(vinyl alcohol) in Water. *J. Phys. Chem. B* **2018**, *122*, 10722.

(60) Oswald, P., Baudry, J., Pirkl, S. Static and Dynamic Properties of Cholesteric Fingers in Electric Field. *Phys. Rep.* **2000**, *337*, 67.

(61) Won, P., Kim, K. K., Kim, H., Park, J. J., Ha, I., Shin, J., Jung, J., Cho, H., Kwon, J., Lee, H., Ko, S. H. Transparent Soft Actuators/Sensors and Camouflage Skins for Imperceptible Soft Robotics. *Adv. Mater.* **2021**, *33*, 2002397.

(62) Nys, I., Stebryte, M., Ussembayev, Y. Y., Beeckman, J., Neyts, K. Tilted Chiral Liquid Crystal Gratings for Efficient Large-Angle Diffraction. *Adv. Opt. Mater*. **2019**, *7*, 1901364.

(63) Lin, I.-T., Choi, Y. S., Wojcik, C., Wang, T., Kar-Narayan, S., Smoukov, S. K. Electro-responsive surfaces with controllable wrinkling patterns for switchable light reflection–diffusion–grating devices. *Mater. Today* **2020**, *41*, 51.

(64) Chu, G., Qu, D., Camposeo, A., Pisignano, D., Zussman, E. When nanocellulose meets diffraction grating: freestanding photonic paper with programmable optical coupling. *Mater. Horiz.* **2020**, ***7***, 511.

(65) Zhang, L., Sun, G., Bai, J., Ma, X., Yin, J., Wang, Q., Jiang, X. Realizing Dynamic Diffraction Gratings Based on Light-Direct Writing of Responsive 2D Ordered Patterns. *ACS Mater. Lett.* **2020**, *2*, 1135.

Supporting Information

Self-Assembly of Twisted Monolayer Cholesteric Films via Surface Tension Local Anisotropy: Implications for Multicolor Optical Tags

Michel Mitov[*]*, Cécilia Boyon, and Vanessa Soldan*†

Email: mitov@cemes.fr

Centre d'Elaboration de Matériaux et d'Etudes Structurales, CEMES, CNRS,

29 rue Jeanne-Marvig, F-31055 Toulouse cedex 2, France.

†Centre de Biologie Intégrative, CBI, Microscopie Electronique Intégrative, METi, CNRS, University of Toulouse, 118 route de Narbonne, F-31062 Toulouse cedex, France.

Table of Contents

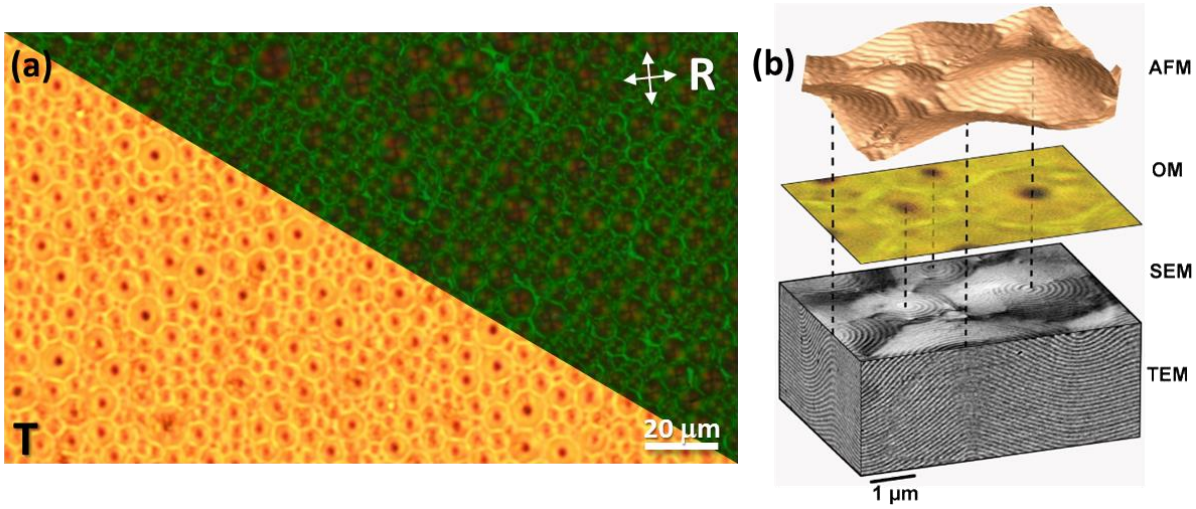

Figure S1. On the polygonal texture. (a) Polygonal cholesteric textures observed in vitrifiable polysiloxane-based oligomers by optical microscopy in transmission (unpolarized light) and reflection modes. The white arrows indicate the orientations of the crossed polarizers in the reflection mode. (b) Tridimensional structure of the polygonal texture obtained by combining different microscopy methods: atomic force microscopy (AFM), optical microscopy (OM), scanning electron microscopy (SEM) and transmission electron microscopy (TEM)[S1]. ©The authors 2011. The dotted lines link polygon vertices. AFM imaging reveals the cone shapes of the polygons, which are the locus of the double-spiral patterns. The relief of conical polygons (height in the 20-100 nm range) results from competition between the surface energy and bulk free energy. The surface tension minimizes the surface area by rearranging the fluid interface from a planar state to a polygonal field[S2]. The energy is lowered by transforming the free surface into a cone, thus reducing the bulk distortion energy at the cost of the surface energy. It should be noted that the formation of a series of valleys and crests at the free surface of the LC films with antagonist anchoring is also observable in nematic LC films[S3]. The double-spiral structures correspond to the adaptation of the cholesteric structure to the relief and anchoring conditions at the limits: rod-like molecules preferentially align tangentially to the substrate and

perpendicularly to the air interface. Close to the air interface, the twisted structure cannot readily adapt to the anchoring conditions. One solution to this boundary problem is the creation of a series of alternating disclination lines at the surface[S4]. Nested arc patterns, as seen in the TEM image, develop because the anchoring at the free surface favors an oblique orientation of the helical axis relative to the surface. Such a situation corresponds to the director distribution with minimum elastic energy, which allows the surface anchoring and bulk planar structure.

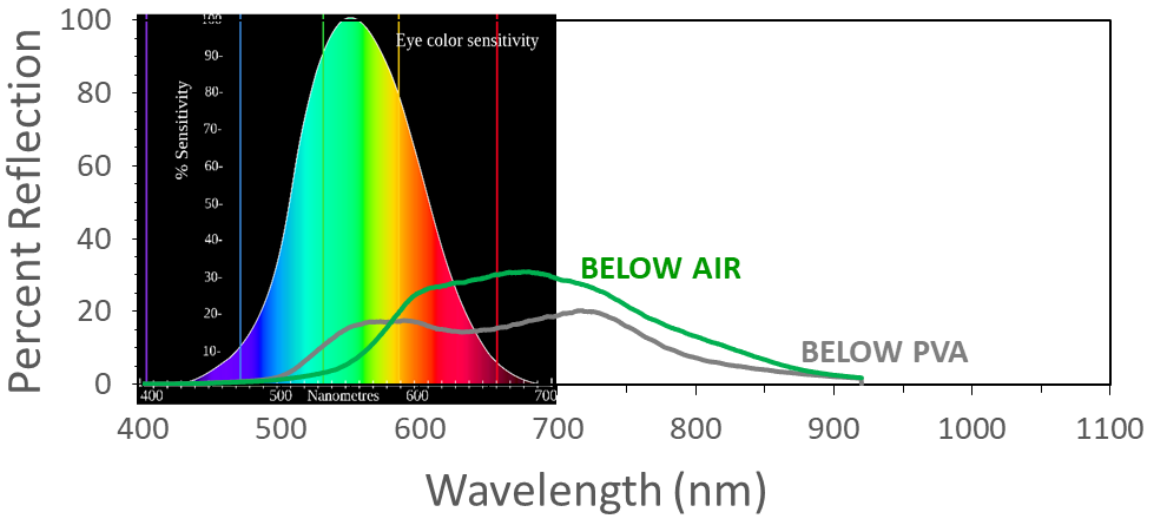

Figure S2. Reflection spectra of the silver and green stripes for an annealing time equal to 15 min *versus* the spectrum of human eye sensitivity. The reflectance assigned to the green–yellow stripe (below air) quickly increases from 510 to 600 nm. This change corresponds to the maximum eye color sensitivity (from 90 to 100%), which is scaled from approximately 530 to 580 nm. (Image of the spectrum of eye sensitivity by Skatebiker and vectorized by A. Rędzikowski. CC BY-SA 3.0).

Discussion on the comparison with glassy samples mimicking the cuticle of *C. gloriosa*. In a previous article on the physics of the cuticle of *C. gloriosa*[S5], we focused our investigations

on biomimicry, *i.e.*, accurately reproducing the optical, structural and functional properties of its striped carapace. We designed a synthetic version in the form of glassy polymeric films. The difference in the reflected colors, from green to silver, was determined solely by the orientation of the helical axes at the surfaces of the open film, which produced different effective pitches, from strongly oblique to perfectly straight lines, in the fingerprint-like texture. No difference in the textural pitch between dissimilar stripes was observed by TEM.

The aims of both studies are different. In the present study, they consist of (i) finding the conditions for multicolor patterning in polymerized films; (ii) organizing pattern formation at the surfaces of crosslinkable films and unsolidified films (to find solutions specific to the soft nature of the surface where a surface tension differential leads to different periodicity distributions in both kinds of stripes); and (iii) laying the foundation for the preparation of single layer, multicolored films with a transmission band that evolves from similar broad bands to two narrow bands with different pitch distributions and amplitudes.

The experimental frameworks of both studies are also different, for example, the mixture formulation of both polysiloxane-based oligomers, their glassy transition temperature (50-55°C for the vitrifying material *vs.* 0°C for the crosslinkable material), and the means to solidify a material with partial open surfaces (by thermal quenching at RT for the vitrifiable material *vs.* crosslinking at 60°C for the crosslinkable materials). Among the differences, we consider the viscosity, which is of paramount importance in the role of tension anisotropy $\Delta\gamma$ in describing phenomena. For example, for the compound that reflects green light, the vitrifiable compound (λ_0 = 540 nm) must be heated to 120°C to exhibit film-forming behavior similar to that of the crosslinkable compound (λ_0 = 500 nm) when heated at 60°C (process temperature of the bilayer). This considerable difference is in agreement with the large gap for T_g values between the compounds. The crosslinkable material is less viscous than the vitrifiable counterpart when both

compounds are in the cholesteric phase. Monomers *c* and *d* (Figure 2 and *LC mixtures* section) are added by the supplier to the oligomers to reduce their viscosity. We thus assume that the vitrifiable compound possesses greater inertia with respect to temperature and environment (surfaces, interfaces, cell gap) due to its intrinsic viscosity, which means that the tension anisotropy $\Delta\gamma$ does not play a major, detectable role in the self-assembly of the bilayer, with or without PVA stripes, during thermal annealing.

Supporting references

(S1) G. Agez, R. Bitar, M. Mitov. Color selectivity lent to a cholesteric liquid crystal by monitoring interface-induced deformations. *Soft Matter* **2011**, *7*, 2841.

(S2) Y. Bouligand, *J. Phys*. Recherches sur les textures des états mésomorphes — Les champs polygonaux dans les cholestériques. 1**972**, *33*, 715.

(S3) P.-G. de Gennes, J. Prost, *The Physics of Liquid Crystals*, Oxford University Press: Oxford, 1993.

(S4) A. Saupe, *Mol. Cryst. Liq. Cryst*. **1973**, *21*, 211.

(S5) A. Scarangella, V. Soldan, M. Mitov. Biomimetic Design of Iridescent Insect Cuticles with Tailored, Self-Organized Cholesteric Patterns. *Nat. Commun*. **2020**, *11*, 4108.